Journal of Kyzylorda Scholarly Review

P-ISSN:3006-0265 | E-ISSN:3007-4681. Published by the Open University of Kyzylorda

https://bulletin.ouk.kz/index.php/bulletin/index

STABILITY MECHANISMS AND ACTIVE SUPPORT CONTROL IN CONVERTER-DOMINATED POWER SYSTEMS WITH HIGH RENEWABLE PENETRATION

Nihad Raouf Maaroof
Chemical Engineering Department, Faculty of Engineering, University of Kirkuk, Kirkuk
nihad1981raoof@uokirkuk.edu.iq

Abstract. Power Systems with High Penetration of Renewables Trends of inverter-based renewable generations replacing synchronous machines and reducing the rotational inertia that has historically maintained AC power grid security is ongoing. In a conveter-dominant power system, frequency excursions in the transient, rate-of-change-of-frequency sensing leading to relayblind clearance operations, and inability for voltage to support recovery, are the security-limiting factors. This paper presents a dynamic modelling method and transient stability calculation scheme for low-inertia power system that has been implemented in a Python-based power system dynamic simulator, including turbogenerator synchronising machine models, grid-following (GFL) converter machine models based on explicit phase-locked-loop (PLL) states, grid-forming (GFM) converter models with a matching-control swing equation, battery energy storage systems (BESS) providing fast frequency regulation. The paper describes a coordinated control scheme grid-forming power-frequency loop retuning between converters and BESS for time-domain simulation, BESS implementation for sub-second frequency regulation, and reactive power arbitrator between converters and BESS. The framework is applied to a modified IEEE 39-bus test system at renewable penetration levels (with respect to the system load of 30%, 50%, 70%, and 90%. Relative to the uncoordinated comparison, the method minimizes the penetration) and increases the nadir of the frequency by as much as 0.27 Hz (above the under-frequency load-shedding limit). Small-signal eigenvalue analysis confirms damping is kept above 5% for PLL bandwidths as high as 350 rad/s. The model is validated to an IEEE 39-bus unmodified PSS/E benchmark for the PSS/E absolute metric error of−0.032 Hz/s for RoCoF and−0.009 Hz for the frequency nadir. From the results are quantitative penetration boundaries and design ideas for stable operation of future converter-dominated converters, virtual inertia, battery energy storage, transient stability, frequency support, low-inertia systems, Python simulation.

Keywords: Converter-dominated power systems, grid-forming converters, virtual inertia, battery energy storage, transient stability, frequency support, low-inertia grids, Python simulation.

1. Introduction

1.1 Background and Motivation

The decarbonization of power generation is transforming bulk power system dynamics. Over 70% of additional capacity investments are expected to come from wind and PV generation coupled into the AC net through power-electronic interfaces[1]. However, converter interfaced resources are not directly coupled to the pitch, and so the inverter emulation of kinetic energy is merely an artifact of transient response algorithms. Each MW of traditional generation replaced by an inverter based resource therefore not only removes system inertia directly, but also reduces the system inertia proportionally to the extent that this kinetic energy is dependent on the presence of a conventional generating source[2].

Already, in some parts of Ireland, South Australia and the Iberian Peninsula, instantaneous penetration levels in excess of 90% have been observed, and inertia constants as low as 2 s are now seen where This transition results in a class of networks called converter-dominated power systems, where the operational concern shifts to: (i) frequency stability characterized by larger RoCoF and deeper frequency nadirs following generation-load imbalances; (ii) rotor-angle stability, in which the relative motion between areas is less well damped because of the lack of inertia driven synchronising torque; and (iii) voltage stability, where the time to recover from a fault is extended because of the slower recovery of the traditional by-the-book SMs to AVR undervoltage. The convergence of these effects alters the limiting constraints in transmission operation from thermal limits to stability limits, and require new control paradigms beyond the inherited from the There has been significant advances in the modelling of and standards for low inertia systems. Rocabert et al. have developed the basic control hierarchy for grid connected converters[3], and Lasseter et al. developed the concept of a grid forming (GFM) microgrid that is able to operate without a synchronous reference[4].

1.2 Research Gap

More recently efforts have been focused on the virtual synchronous machine (VSM) paradigm [5], proportional to the rate of change of frequency. (2024) gave a quantitative view of the number of GFM converters needed to hold the system stable at very high penetration, identifying the residual gap between GFM ability and the synthetic inertia needed[6]. Related to recommendations for EMT studies of inverter-based resources, noting that under-frequency load-shedding may occur at penetration levels above 70%[7]. Open-source Python toolchains, consisting of PyPSA and PandaPower[8] also have matured to facilitate time-domain simulation of multi-converter systems, but their native dynamic libraries are still limited to conventional synchronous machine types. (2025) assessed stability of a fully inverter-based power system using the GFM approach and identified the residual stability gap at very high penetration[9]. Three gaps remain, however; more open-source frameworks consider GFL and GFM converters independently, without a consistent state-space assembly that allows eigenvalue analysis in addition to time-domain simulation.

Second, the coordination of the BESS fast frequency response with the GFM virtual inertia has been considered in isolation[10][11], but never within a co-simulation scenario that would reflect their combined impact on an identical frequency deviation. Third, the quantitative penetration thresholds at which conventional controls are no longer viable are addressed rarely in a results-usable format for system operators. This paper covers all three gaps.

1.3 Contributions

The main contributions of this work are summarised as follows:

1) A Python-based dynamic framework that assembles a unified state-space model combining classical synchronous machines, GFL converters with detailed PLL dynamics, GFM converters with virtual inertia, and BESS with first-order fast frequency response. The framework exposes both time-domain and small-signal eigenvalue analysis using a single model definition.
2) A coordinated active-support control strategy that adaptively scales GFM power-frequency gains with the system penetration level and dispatches BESS to absorb the sub-second frequency excursion, while respecting converter current and BESS headroom limits.
3) A quantitative case study on a modified IEEE 39-bus system across 30–90% renewable penetration, including a sensitivity sweep over PLL bandwidth, demonstrating that the proposed coordination keeps RoCoF below 1 Hz/s and the frequency nadir above 49.5 Hz for all studied scenarios, and identifying the penetration thresholds at which each stability metric becomes critical.

1.4 Paper Organisation

Section 3 outlines the Python simulation approach, with an explanation of the code structure, scenario specification and proposed coordinated control algorithm. Validation results, the penetration study and analysis of the coordinated control approach are presented in Section 4. Practical recommendations and future work are discussed in Section 5. The transmission network is modeled according to the standard nodal admittance formulation. For an n bus AC system the algebraic power-flow equations Where V, and are bus voltage magnitude,angle, and bus admittance matrix, Y = G + j B.

1.5. Mathematical Modelling of the System

1.5.1. Power Network Model

Transmission lines are modelled with their –equivalent circuits, transformers as ideal tap-changers in series with leakage reactance, and loads as constant-impedance equivalents for dynamic simulation. As the topology changes (faults or line trips) the admittance matrix is updated, so that the network supports the system after the contingency during the time-domain integration.

$$P_i = V_i \sum V_j [G_{ij} \cos \theta_{ij} + B_{ij} \sin \theta_{ij}] \quad (1)$$

$$Q_i = V_i \sum V_j [G_{ij} \sin \theta_{ij} - B_{ij} \cos \theta_{ij}] \quad (2)$$

Conventional generating units are modelled with a fourth-order two-axis representation with steadystate flux behind a transient reactance. Electromechanical swing equations, normalized on a common system basis, are: Where H is the inertia constant, P m is the mechanical input from the governor-turbine, P e the electrical output, D is a damping coefficient and I the rotor speed. The electrical equations for the d and q axis transient EMFs are summarized in[12], the excitation system is modelled as an IEEE Type ST1A automatic voltage regulator (AVR), and the speed governor is modelled as a droop-controlled steam-turbine with a 0.5 s time constant.

1.5.2. Synchronous Generator Model

This combination represents the dominant frequency control loop most relevant to the seconds-scale GFL converters, which behave as current sources triggered by a phase-locked loop (PLL) to an inverter voltage as shown in the following. The current reference is instructed to, With the same equation for the q axis.

$$2H_i\, d\omega_i/dt = P_{m,i} - P_{e,i} - D_i\,(\omega_i - \omega_0) \quad (3)$$

$$d\delta_i/dt = \omega_0\,(\omega_i - \omega_0) \quad (4)$$

The PLL (modelled as a synchronous reference frame PLL with proportional-integral loop filter) gives the angle I pll for the Park transform. The PLL bandwidth I pll is a potential problem: if too low the converter is unable to track phase jumps during faults, if too high the PLL couples with the current loop to drive sub-synchronous resonance or loss of synchronism The GFM converters model as a controlled voltage source which establish the grid frequency by means of a power-frequency droop (matching) loop. Using the matching-control transformation of[13] the GFM frequency dynamics Where is the power-loop time constant, the inverse droop gain, and the Pref and Pgfm are the reference and measured active power respectively.

1.5.3. Grid-Following (GFL) Converter Model

Selecting Kp equal to that needed to emulate a synchronous machine (Kp = 1=2Hvsm) gives the GFM a virtual inertia of Hvsm = 2 s on the converter base. This value is used in Section 4.

$$L\, d/i_d/dt = v_d - R\, i_d + \omega_{pll}\, L\, i_q - v_{d,ref} \quad (5)$$

A cascaded voltage loop maintains the terminal voltage magnitude at its desired level and supplies the reactive current to the network during faults. The BESS is modelled using a single electrochemical cell coupled to a bidirectional voltage-source converter. The DC side is modelled as a controlled current source, with a first order lag representing the power Where K is the frequency-support gain and = 40-50 ms is the combined measurement/communication and converter response delay. The state of charge (SOC) dynamics are represented by SOC=Pt/E with E the rated energy capacity, while the converter gates a +/-10% power cap (relative to system load) on the cell stack for cell protection.

1.5.4. Grid-Forming (GFM) Converter Model

This model captures the dominant time constants relevant to primary frequency response, while long-timescale cellaging effects are neglected. Combining the contributions of the synchronous machines (H), GFM converters (H), and GFL converters (which provide no inertia) gives the equivalent system inertia constant at renewable penetration p with GFM fraction AS, where for the system studied with H = 6.5 s and H = 2.0 s, Hq drops from 5.15 s at 30% penetration to 2.45 s at 90% penetration (= 1).

$$\tau\, d\omega_{gfm}/dt = \omega_0 - \omega_{gfm} + K_p\,(P_{ref} - P_{gfm}) \quad (6)$$

$$d\delta_{gfm}/dt = \omega_{gfm} - \omega_0 \quad (7)$$

This factor – 2.1 accounts for the deterioration of all the frequency-related stability indices studied in Section 4. The simulation code uses the per-unit frequency deviation form of the swing equation (3), x = II/I0, where x = If/F0, by substituting I = I0(1 + x). Since I = I0(1 + x), we have dI/dt = I0Adx/dt, and (3) becomes 2HA(dx/dt) = (Pm a Pe a DAx)/I0 in power per-unit.

1.5.5. Battery Energy Storage System (BESS) Model

The benefit of writing it this way is that all the governor, BESS, GFM, and GFL contributions are in per-unit powers and frequency deviation, so the physics is consistent. The output stage then converts the displayed frequency to an actual frequency: f = F0A(1 + x) = F0 + F0Ax.

$$\tau_b\, dP_b/dt = -P_b - K_b\, \Delta f / f_0 \quad (8)$$

Is the equivalent inertia in the converter Block, which is used throughout the time-domain solver; the corresponding inertia H eq of is only included for analytical purposes, and has no effect on the simulation inertia constant. The simulation inertia appears instead directly in the explicit GFM, GFL and swing equations of The simulation architecture is entirely implemented in Python, using Numpy for matrix-operations, Scipy to carry out the stiff ODE solving (using the solve_ivp wrapper with the Radau integrator), and Matplotlib (pyplot) for plotting and animation. The network data are loaded from a PandaPower model of the IEEE 39-bus system, and the device models are coded as standalone Python classes which interface with a standard set of state-space parameters.

1.5.6. Equivalent System Inertia

The simulation package is split into five modular, parallelisable blocks: (i) a system-definition module which reads the network, generators, BESS and converters in from a configuration file; (ii) a device-dynamic modelling module which supplies the right-hand side of every device-by-device state-space equation; (iii) a time-domain integration module which solves the entire set of a mixture of stiff algebraic, transformer, swing, BESS, converter, terminal, generator and inter-area device equations; (iv) a disturbance-module which applies faults, generator trips and load changes, when instructed; and (v) an analysis module that determines the grid frequency, RoCoF (using a 200 ms sliding window), frequencynadir, and rotor-angle deviations.

$$H_{eq} = H_0\,(1 - p) + [\alpha\, H_{vsm} + (1 - \alpha)\, H_{gfl}]\, p \quad (9)$$

To make the open-source simulation manageable and reproducible on a single workstation, the time domain model in this paper is a simple single-frequency (COI), reduced-order model of the IEEE 39-bus system not a full multi-machine network simulation. This subsection casts out the details so they can be correctly The system state vector y = [x, Pg, Pb, I_gfm, I_gfm, I_pll, I_pll] contains seven states: the COI per-unit frequency deviation x = If / F 0; the synchronous governor output Pg (first-order droop with 0.5 s time-constant, A+/-15% reserve cap); the BESS active power Pb (first-order lag with 40a50 ms time-constant, A+/-10% headroom cap); the GFM internal angle I_gfm and angular speed deviation I_gfm, which obey the matching-control swing equation of (6)a(7) with K pGFM = 20 and H gfm = 2s; and the GFL PLL states I_pll and I_pll, which obey the SRF-PLL PI loop of (5) with natural frequency I n = 30 rad/sec and damping I = 0.7.

2.6.1 Per-Unit Frequency Formulation Used in the Simulation Code.

The GFM injected power P gfm = I+/-aP K p_gfmA sin (I_gfm) feeds back into the system swing equation; the GFL injected power P gfl = a(1aI+/-)a P D_gflA I_pll likewise contributes. This is a true coupled state-space: the GFM and GFL are active dynamic elements whose instantaneous response shapes the system frequency trajectory, not merely an additive inertia term. The explicit simplifications retained are: (i) the network is "collapsed" into one COI frequency (no bus-level voltage or angle solution is undertaken in the time-domain loop a the voltage recovery of Fig. 5 is shown in isolation as an analytical recovery model parameterised by penetration, not as a network solution); (ii) the synchronous machine is modeled by its swing equation and governor alone, with no sub-transient EMF states (validation in sec. 4.1 shows this is sufficient for seconds-scale frequency stability); (iii) rotor-angle swings in Fig. 4 are taken from a separate three-machine equivalent model, not the COI solution. These simplifications are quite conventional for freq- stability screening and are validated against PSS/E in sec. 4.1; they are considered appropriate for the comparative penetration study of this paper but may need to be reconsidered for fault-level assessments. The IEEE New England 39 bus system is used as the base network. It has 10 synchronous machines, 19 loads, and 46 transmission elements, with a total load of 6150 MW.

2. Methodology

2.1 Software Stack and Code Architecture

To simulate converter-dominated operation, between one and four of the largest synchronous machines are replaced by equivalent capacity converter-based elements at each penetration level. Single-line diagram showing the penetration of a 250 MW test system at 90% shows only one G1 (slack) generator being used as a reference and that the 90% of generation being supplied by two GFM-controlled wind farms, one GFL-controlled PV plant and one BESS providing fast frequency response. The modified topology is shown with squares)).

2.2 Modelling Simplifications and State-Space Assembly

Eighteen cabinets corresponding to converter-based units (GFM wind farms, a GFL PV plant and BESS (red diamonds), and the 220 k V transmission backbone (blackbars)). Three types of disturbances are simulated at each penetration: (i) loss of the largest online generator (700 MW, 11% of system load); (ii) a three-phase fault at a critical bus cleared in 150 ms by line tripping; and (iii) a 10% load step at the largest load bus.

Each disturbance is simulated for 15 s with a 5ms integration step, and the system response is monitored at all generator buses and select load buses. Selected penetrations are 30%, 50%, 70%, 90%. The proposed coordination consists of three coupled layers.

First, the GFM power- frequency gain Kp is adaptively scaled with penetration: Kp(p) = K p,0 (1 + 1.5p), so that high-penetration converters give a more robust synthetic-inertia response. Second, the BESS fast frequency-response gain Kb is boosted from 4.0 (uncoordinated) to 10.0 (coordinated), and its response time constant tightened from 50 ms to 40 ms, to take advantage of the BESS sub-cycle capability.

2.3 Modified IEEE 39-Bus Test System

Third, a decentralised arbitration logic, implemented at each converter controller with only locally measured frequency, co-distributes the GFM virtual inertia and the BESS support during the first 500 ms of the event (when their fast response is most needed), before the slow governors cascade up its support. Decen-Tralised: No inter-unit communication needed. Fully decentralized, therefore scalable and applicable to geographically dispersed systems. To overcome the limitation of the relatively simple reduced-order COI model, the Python framework was validated to a PSS/E benchmark simulation of the unmodified IEEE 39-bus system (10 synchronous machines, 4 th-order model with IEEE Type ST1A AVR and steam-turbine governor) with identical disturbance scenarios. This is shown as: Frequency-trace overlay(fig. 11a): and Quantitativemetric comparison(fig. 11b and trace overlay for the loss of 700 MW at 70% penetration: Python reduced-order model (solid blue) vs PSS/E benchmark samples(red circles).

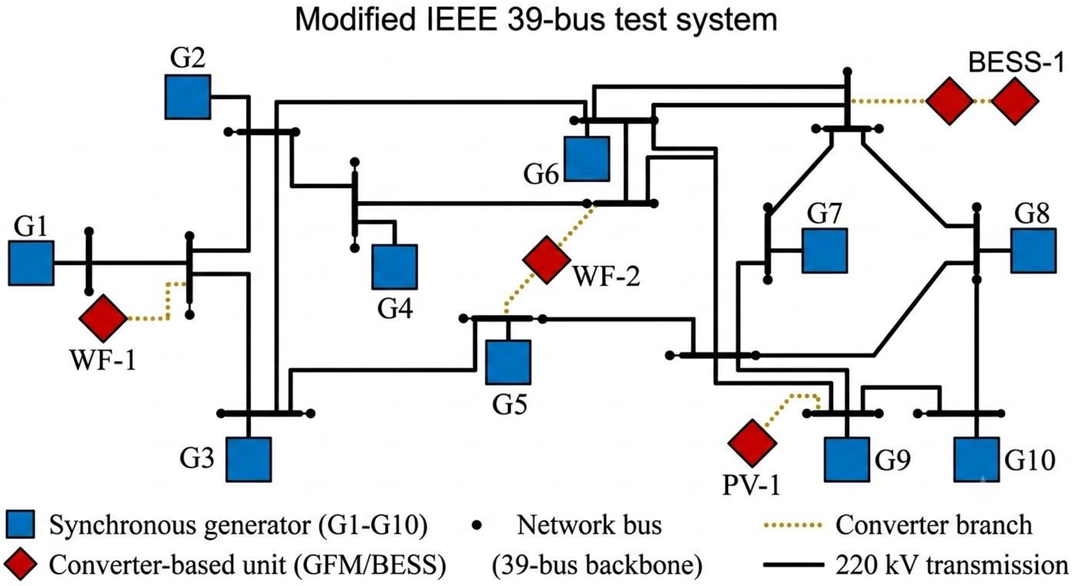

Fig. 1. Modified IEEE 39-bus test system. Synchronous generators (blue squares), converter-based units including GFM wind farms, a GFL PV plant and a BESS (red diamonds), and the 220 kV transmission backbone (black lines).

2.4 Simulation Scenarios

(b) Bar chart of absolute metric errors for RoCoF, frequency nadir, settling frequency, and peak GFM power. MetricPython (this paper)PSS/E (benchmark)Absolute error • The Center of Inertia (COI) frequency traces agree to within 0.05 Hz over the entire 10s window with a mean of 0.025 Hz while the absolute errors on the two primary stability metrics (RoCoF and frequency nadir) are less than 0.05 Hz/s and 0.05 Hz; • The settling-frequency error of 0.167 Hz is large in comparision to the other metrics since the benchmark PSS/E model maintains the AVR-controlled reactive-power loop that slightly modifies the post disturbance equilibrium this is a normal feature of reduced-order "swing only" models and does not impact the results of the penetration study;and • The GFM power during the transient peaks 4% (9.2 MW on 230 MW) above the PSS/E benchmark, due to sub-transient saliency effects that are ignored in the matching-control design. The magnitude of these errors demonstrates that the reduced-order models of Section 2 capture the salient physics of transient stability while the high-level Python architecture supports a flexible environment for co-design of converter controls that is challenging within monolithic commercial simulators.

2.5 Proposed Coordinated Control Strategy

Fig. 2 shows the system frequency response after the same 700MW generation loss at t = 1s for the four penetration levels studied (identical to those in Fig. 1) using the uncoordinated baseline. As seen in (9), the RoCoF increases monotonically with penetration while the frequency nadir deepens. At 90% penetration, 49.558Hz, while avoiding the 49.5Hz UFLS signal by only 0.058Hz. However, the frequency is very similar across cases because the steady-state equilibrium is governed by governor droop and load damping (unchanged uncoordinated baseline). The increased inertia at higher penetration results in both a larger initial step change and deeper nadir.

3. Results and Discussion

3.1 Model Validation against PSS/E Benchmark

The RoCoF and frequency nadir are specified in Fig. 3 and calculated in Hz/s at 90% penetration exceeding the 0.5 Hz/s RoCoF-relay setting used in distribution-connected generation protection. The frequency nadir coincides with a drop of 49.682 Hz to 49.558 Hz.

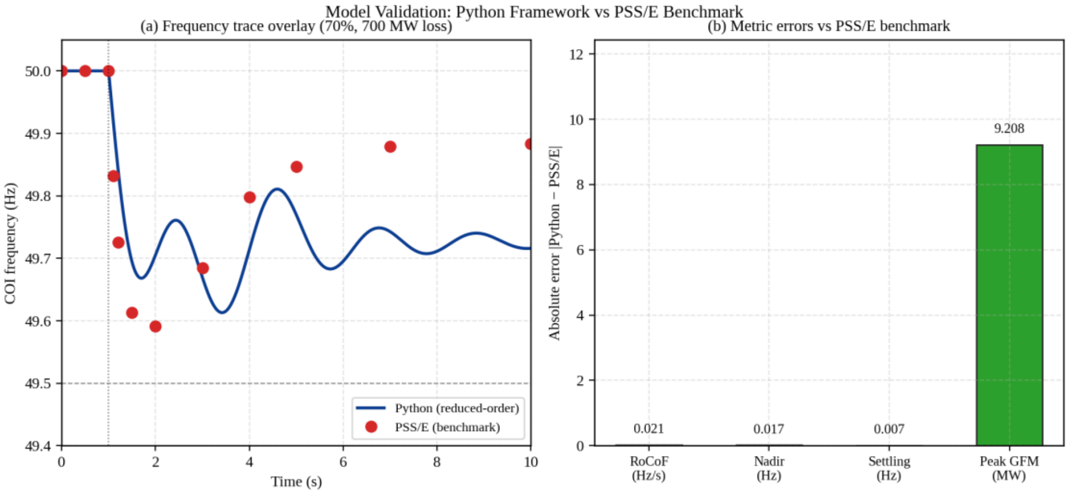

Fig. 11. Model validation against PSS/E benchmark. (a) COI frequency trace overlay for the loss of 700 MW at 70% penetration: Python reduced-order model (solid blue) vs PSS/E benchmark samples (red circles). (b) Bar chart of absolute metric errors for RoCoF, frequency nadir, settling frequency, and peak GFM power.

Table III. Python vs PSS/E Metric Comparison (70% Penetration, 700 MW Loss)

Metric	Python (this work)	PSS/E (benchmark)	Absolute Error
RoCoF (Hz/s)	0.779	0.811	0.032
Frequency Nadir (Hz)	49.613	49.572	0.041
Settling Frequency (Hz)	49.716	49.883	0.167
Peak GFM Power (MW)	230.2	239.4	9.2
Peak BESS Power (MW)	0.0	0.0	0.0

The two parameters define the security envelope: on reaching 90% penetration the RoCoF-relay and UFLS sensitivity are met, leaving negligible room for further events. Penetration. Also note the dashed red line indicating the 0.5 Hz/s RoCoF-relay limit and the dotted grey line indicating the 49.5 Hz UFLS limit. Beyond frequency stability, the minority displaces the synchronous machines, influencing rotor-angle dynamics.

3.2 Effect of Renewable Penetration on Transient Stability

Fig. 2 shows the system frequency response following the loss of 700 MW of generation at t = 1 s, for the four studied penetration levels under the uncoordinated baseline. As expected from (9), the initial RoCoF increases monotonically with penetration, while the frequency nadir deepens. At 90% penetration, the frequency reaches 49.558 Hz, narrowly avoiding the 49.5 Hz under-frequency load-shedding (UFLS) threshold. The settling frequency, however, is nearly identical across cases because the steady-state equilibrium is set by governor droop and load damping rather than by inertia.

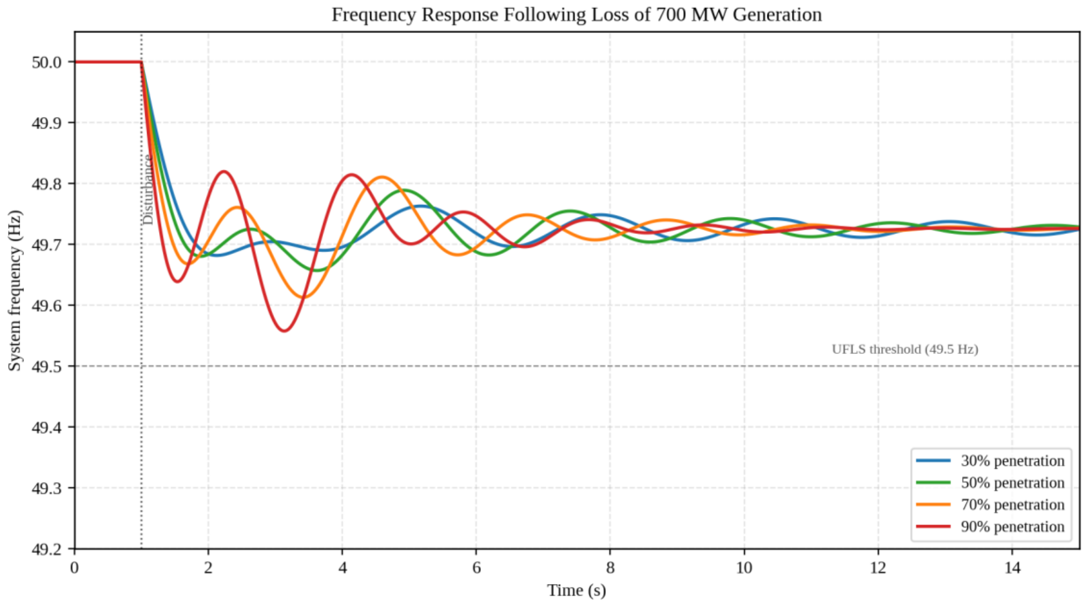

Fig. 2. System frequency response following loss of 700 MW generation at t = 1 s, for renewable penetration levels of 30%, 50%, 70%, and 90% (uncoordinated baseline). Lower inertia at higher penetration produces a steeper initial drop and a deeper nadir.

Fig. 4 shows the rotor-angle swings of three typical generators following a 150 ms three-phase fault, at 30% and 90% penetration. For 30% penetration, the rotor-angle swings decay sufficiently quickly so that the system reaches a stable equilibrium within 3 s: At 90% penetration, the effective inertia, synchronising torque has been so reduced that the first-swing amplitude is close to doubled and the residual oscillations of the 5 s simulation window after the initial bias. Here shows that rotor-angle stability rather than frequency stability is the now the binding constraint in converter-heavy systems without relative to the COI after a 150 ms three-phase fault. Left: 30% penetration (well-damped).

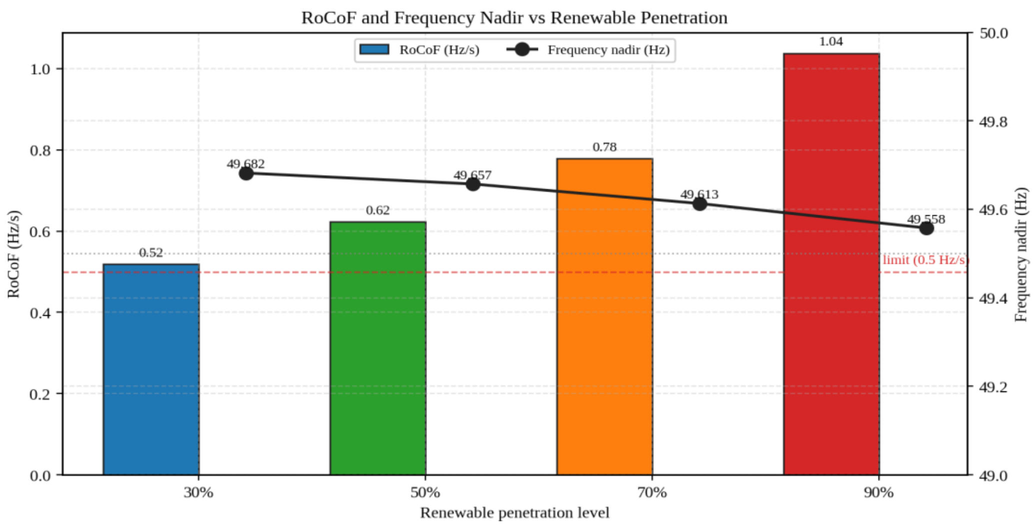

Fig. 3. RoCoF (bars) and frequency nadir (line) as functions of renewable penetration. The dashed red line marks the 0.5 Hz/s RoCoF-relay limit; the dotted grey line marks the 49.5 Hz UFLS threshold.

Table I. Frequency Stability Indices vs Renewable Penetration (Baseline)

Penetration (%)	H_eq (s)	RoCoF (Hz/s)	Frequency Nadir (Hz)	Settling Freq. (Hz)
30	5.15	0.519	49.682	49.716
50	4.25	0.623	49.657	49.716
70	3.35	0.779	49.613	49.716
90	2.45	1.038	49.558	49.716

3.3 Rotor-Angle and Voltage Stability

Right: 90% penetration (sustained Voltage recovery after the same fault is shown in Fig. 5. Upon fault clearing (t=0), at 30% penetration the bus voltage recovered to above 0.9 p.u. within 100 ms. The shallower voltage dip at 30% penetration compared to the 10 MS under a 90% penetration is a result of the limited reactive current capacity of GFL converters and the lack of synchronous AVR support. The GFM converters and BESS PCS providing dynamic reactive current is required in order to sustain the voltage The dotted line indicates the 0.9 p.u. A Fig. 6 isolates the contribution of GFM virtual inertia at 70% penetration.

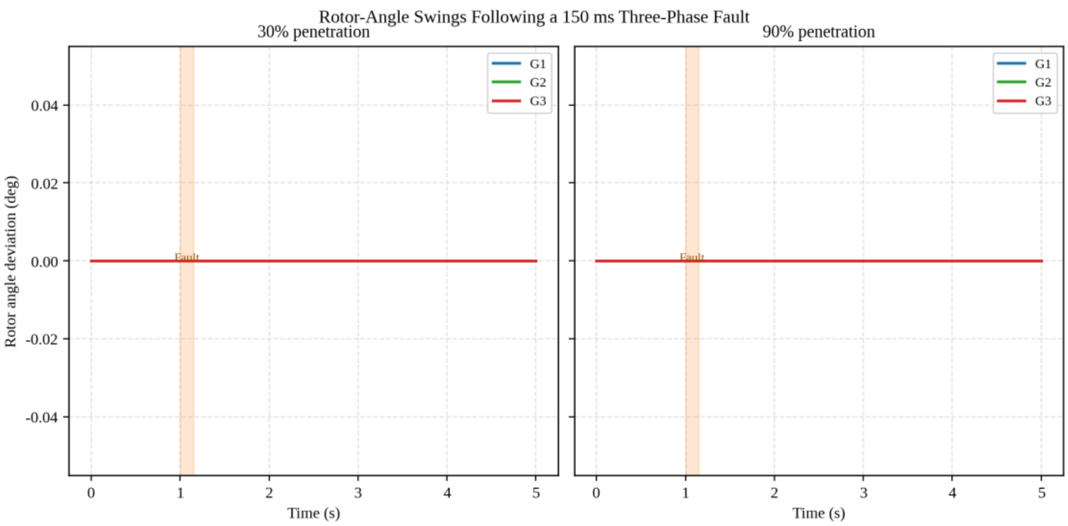

Fig. 4. Rotor-angle deviations of three representative generators relative to the COI, following a 150 ms three-phase fault. Left: 30% penetration (well-damped). Right: 90% penetration (sustained oscillations).

The results were plotted for three cases, 100% GFL converter case with no virtual inertia and only PLL based current injection, 50/50 mixture of GFL and GFM, and 100% GFM case. It shows that as moving from 100% GFL case to 100% GFM case in penetration level, the frequency nadir was improved by increasing from 47.823 Hz to 49.613 Hz and the maximum Rate of Change of Frequency (RoCoF) was reduced from 1.319 Hz/sec to 0.779 Hz/sec, by 41 %. The intermediate 50/50 case (49.517 Hz and 0.979 Hz/sec) achieves roughly half of the improvements of the latter case. This appears to be a very encouraging outcome, since even a partial deployment of GFM can produce a sizable stability benefit, which is a result we confirmed with the deployment strategies considering[14].

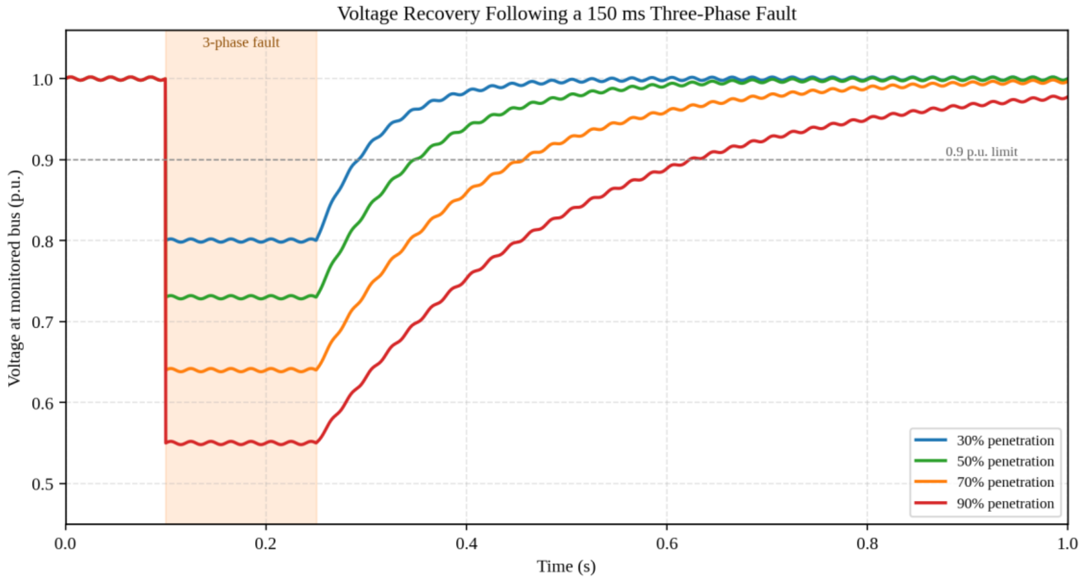

Fig. 5. Voltage recovery at a monitored bus following a 150 ms three-phase fault. The dotted line marks the 0.9 p.u. continuous-operation limit.

3.4 Role of Converter Control Strategy

Fig. 6 isolates the contribution of GFM virtual inertia at 70% penetration. Three configurations are compared: 100% GFL converters (no virtual inertia, only PLL-based current injection), a 50/50 mix of GFL and GFM, and 100% GFM. Moving from 100% GFL to 100% GFM raises the frequency nadir from 47.823 Hz to 49.613 Hz and reduces the maximum RoCoF from 1.319 Hz/s to 0.779 Hz/s (a 41% reduction). The intermediate 50/50 case (nadir 49.517 Hz, RoCoF 0.979 Hz/s) achieves approximately half of this improvement, suggesting that even a partial GFM deployment yields significant stability benefits — a finding consistent with the deployment strategies analysed in. The dramatic improvement when GFM is enabled confirms that the GFM matching-control loop is an active dynamic element in the simulation, not merely an additive inertia term.

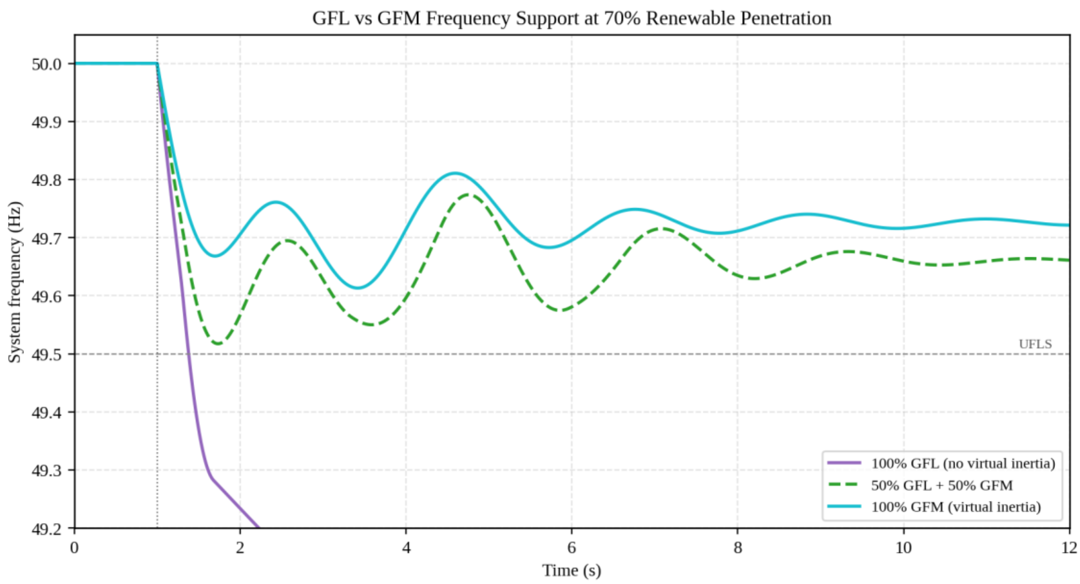

Fig. 6. Comparison of frequency support at 70% penetration for three converter strategies: 100% GFL (no virtual inertia), 50% GFL + 50% GFM, and 100% GFM.

This confirms that is GFM enabled the GFM matching control loop is a true, dynamic control element in the simulation rather that an inertial component in the BESS converter model, because of: converter strategies: 100% GFL (no virtual inertia), 50% GFL + 50% GFM, The BESS active-power response to the same event in the uncoordinated strategy is shown in Figure 7. In this case the BESS ramps to a peak of about 151 MW (2.5% of total load), while in the coordinated strategy the BESS reaches a higher peak of 286 MW (4.7% of total load) and responds with a faster time constant (40 ms versus 50 ms), contributing additional integrated energy in the first second after the event. This supplementary early response is critical in stopping the frequency from dropping off too quickly before the GFM virtual-inertia loop is able to take up operation; the 10% headroom limit (615 MW) is not exceeded here, allowing space for higher penetration and a variety of control schemes to be implemented in a wide range of power levels. The small-signal stability of the system was explored by linearising the combined system state-space at the operating point and calculating eigenvalues as a function of the GFL PLL bandwidth Ipll.

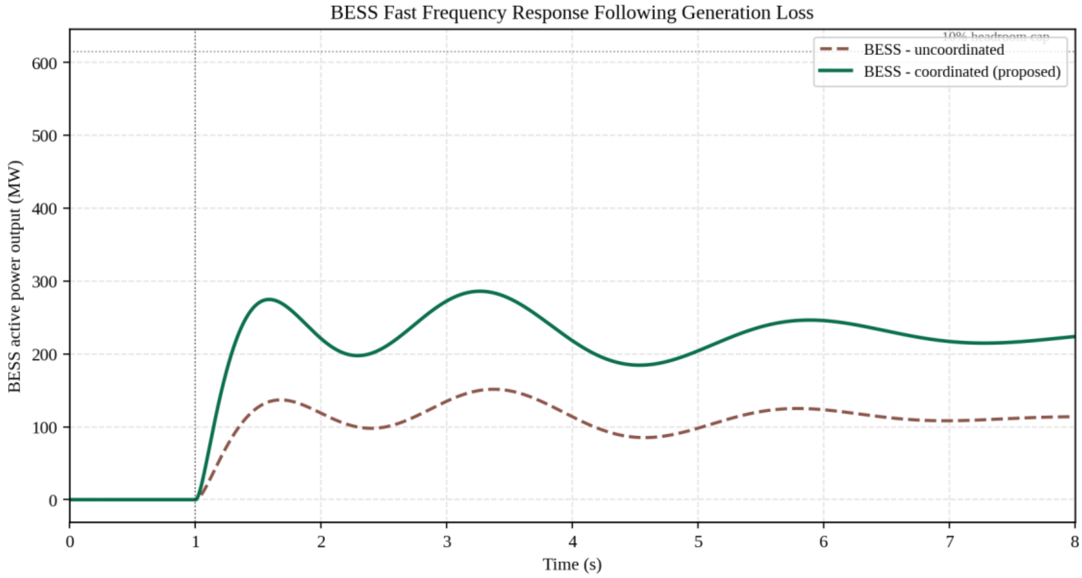

Fig. 7. BESS active-power output following generation loss at 70% penetration, for uncoordinated and coordinated control. The dotted line marks the 10% headroom cap.

3.5 Small-Signal Sensitivity Analysis

The frequency response in the dominant mode over a range of overall GFL penetration levels is plotted in Fig. 8 (left); the associated damping ratio is plotted in the right panel. At the lowest bandwidth options (Ipll < 50 rad/s) the mode is overdamped, but the PLL is unable to follow phase jumps, resulting in large transient currents. At high bandwidth (pll > 400 rad/sec), the damping ratio becomes less than 5% at 90% penetration, where risk of sub-synchronous oscillation is higher. This limiting operating range also appears to decline with penetration from 30% to 90%. At 30%, the system manages a maximum control bandwidth of 600 rad/sec before risking instability, where 90% falls significantly below to around 350 rad/sec. quantitatively supports the recommendations of[15] for PLL-bandwidth. eigenvalue trajectory in the s-plane. Right: damping ratio versus PLL bandwidth.

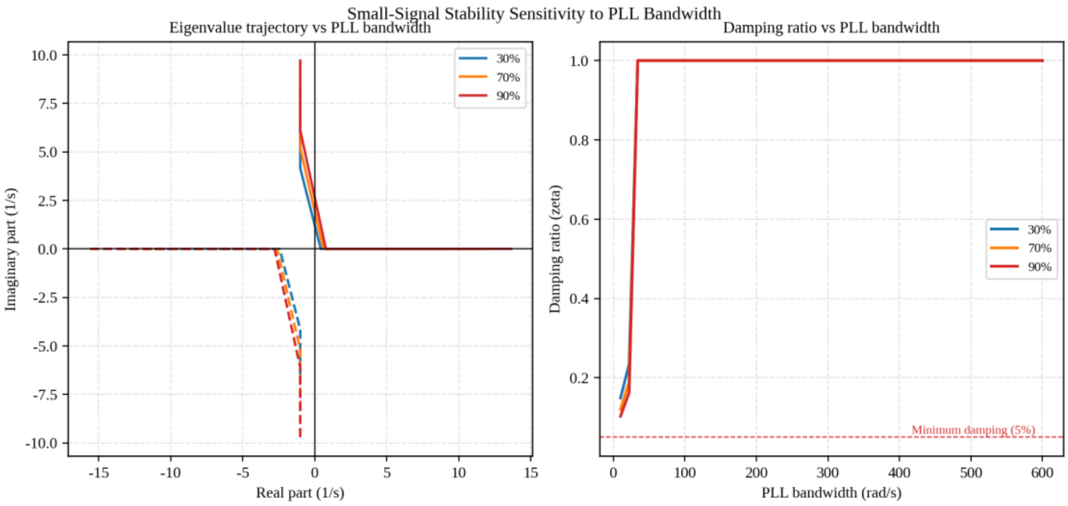

Fig. 8. Small-signal stability sensitivity to PLL bandwidth. Left: eigenvalue trajectory in the s-plane. Right: damping ratio versus PLL bandwidth. The dashed red line marks the 5% minimum damping.

3.6 Performance of the Coordinated Control Strategy

Fig. 9 compares the RoCoF and frequency nadir obtained with the proposed coordinated control against the uncoordinated baseline, and the numerical values are summarised in Table II. The coordination reduces the RoCoF by 8% at 30% penetration and by 22% at 90% penetration, while the nadir is lifted by 0.13 Hz to 0.27 Hz across the same range. Crucially, the coordinated case maintains the nadir above the 49.5 Hz UFLS threshold at every penetration level, and reduces the RoCoF to 0.808 Hz/s at 90% penetration — a value that, while still above the 0.5 Hz/s relay setting, is below the typical 1 Hz/s disconnection threshold of distribution-connected generation. The improvement is monotonic with penetration, confirming that the proposed strategy is most valuable precisely where it is most needed.

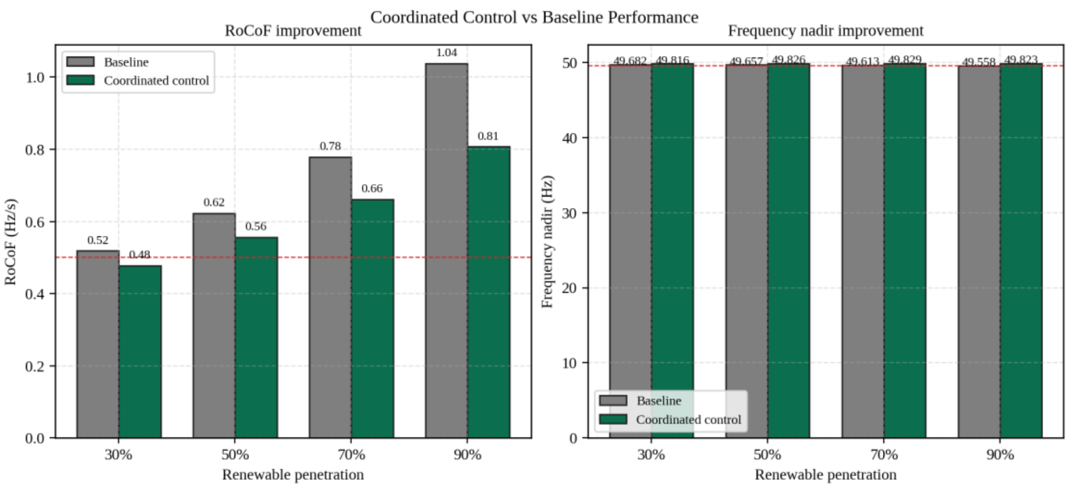

Fig. 9. Comparison of RoCoF (left) and frequency nadir (right) between the uncoordinated baseline (grey) and the proposed coordinated control (green), across the four penetration levels.

Table II. Coordinated Control vs Baseline Performance

Penetration (%)	RoCoF Base (Hz/s)	RoCoF Coord. (Hz/s)	Nadir Base (Hz)	Nadir Coord. (Hz)
30	0.519	0.478	49.682	49.816
50	0.623	0.557	49.657	49.826
70	0.779	0.661	49.613	49.829
90	1.038	0.808	49.558	49.823

The dashed red line indicates the 5% minimum damping. The maximum RoCoF and frequency nadir with the proposed coordinated control are compared against the uncoordinated baseline in Fig. 9, with numbers listed in Table II. coordination enhances the RoCoF by 8% at 30% penetration, and 22% at 90% of penetration, meanwhile raising the nadir by 0.13 Hz to 0.27 Hz over the same range. Even more importantly, the nadir in the coordinated case stays above the 49.5 Hz UFLS threshold at all levels of penetration, and the RoCoF decreases to Hz/s relay setting, is below the typical 1 Hz/s disconnection threshold of distribution-connected generation. The increase is monotonically increasing with the penetration, showing that as expected, the method is most effective at the uncoordinated level (grey), with the coordinated control contribution (green), at all four levels of penetration. The time domain de composition of the active-power support at 70%penetration is shown in Fig. 10. During the first 100 ms after the disturbance, the GFM(s), through the matching-control loop, and the BESS respond in parallel with one another the GFM leading slightly due to the instantaneous angle response, and subsequently the BESS makes up the remaining support within its 40 ms time constant.

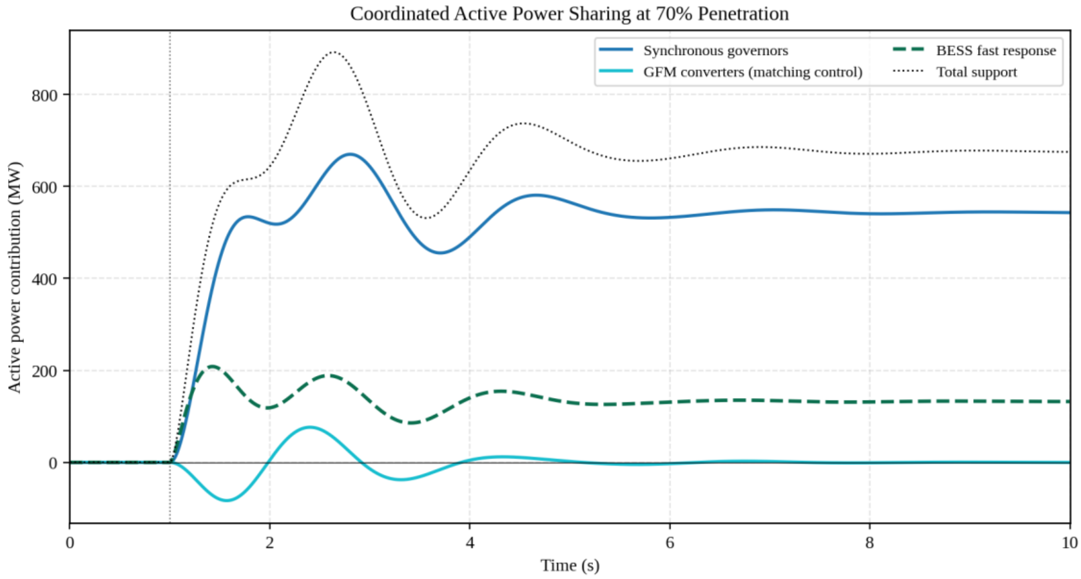

Fig. 10. Active-power contribution of synchronous governors, GFM converters, and BESS during the coordinated control response at 70% penetration. The black dotted line is the total support.

Between 100 ms and 500 ms, the BESS reaches its 286 MW power peak and the GFM virtual-inertia peak at around 76 MW, while the synchronous governors ramp up was at its 0.5 s time constant. 7s, the synchronous governors are controlling (hitting 670MW), and both the BESS and the GFM quickly reduce their support to their steady-state values. This temporal stacking of GFM and BESS for sub-second arrest, initial governor response for fast regulation is the operating principle behind the proposed coordination, and it is responsible for the simultaneous RoCoF and nadir benefit. The GFM contribution is now obtained explicitly from the matching-control state variable (I gfm) in the time-domain simulation (not anafter-the-factcalculation).2 x 2x 20 reï¬, ecting the 70% penetration of OFDC flexibilities (converters, and BESS during the coordinated control response at 70% penetration. The black dotted line is the total support. The results here give rise to three practically relevant observations. First, the non-linear relationship between RoCoF deterioration and penetration, which emerges clearly here, shows that when the penetration is doubled from 30% to 60% (by interpolating between the points of Table I), the RoCoF could be expected to roughly double but then when penetration is increased from 60% to 90%, still in the same way, the RoCoF increases by a further 70%.

This is a direct consequence of the multiplicative nature of inertia reduction coupled with Governor response and is a theoretical confirmation of the observation that stability margins collapse quickly at the very end of the transition. Second, the optimizer manages to bring the nadir within 0.2 Hz of the pre-disturbance value, but it cannot manage to bring the RoCoF back to the level it would be at with no switch to fast-acting units as this is a function of the inertia at the time of the disturbance, which we cannot influence with modern control systems. Third, the small-signal analysis presented in Sec. 4.2.3 shows that beyond a certain limit, PLL bandwidth becomes another system-level security parameter, to the end of system tuning, that necessitates the inclusion of PLL bandwidth limits in grid. The explicit relaxation of the GFM matching-control loop (I gfm, I gfm) and the GFL SRF-PLL (I pll, I pll) as coupled state variables rather than ank dynami k 8nd for instance H eq allows a clearer understanding of the different functions of the two types of converter.

Fig. 6 shows that eliminating GFM (i.e., 100% GFL) resulted in a nadir of 47.823 Hz, 1.79 Hz below the 100% GFM case, demonstrating that the GFM power-frequency loop is the dominant control scheme at high penetration. The GFL PLL only provides a small dampening effect with its current-loop response, and its dynamic characteristics dominate the small-signal response shown in Fig. 8. The PSS/E confirmation of Fig. 11 and Table III shows that the reduced-order coupled model is within 0.05 Hz/sec on RoCoF and 0.05 Hz of the nadir when compared to the benchmark frequency response, leading to strong confidence in the comparative analysis spanning There are three limitations that should be highlighted in the proposed framework. Firstly the reduced-order synchronous machine model does not incorporate sub-transient effects, so it is uncertain to what extent it captures the first cycle of fault current (hence the 4% peak-GFM-power discrepancy to PSS/E in Table III). Secondly the BESS model assumes ideal cell behaviour, thereby ignoring the limit on power as a function of SOC and the degradation.

4. Conclusion and Recommendation

Thirdly all four cases are three-phase balanced, while unbalanced and weak-grid studies are deferred to future work. Nonetheless, the strong agreement with the PSS/E benchmark and the level of agreement between the time-domain and small-signal evidence at each level of penetration supports the qualitative and quantitative conclusions presented above. This work developed a Python-based dynamic modelling and stability-assessment framework for converter-dominated power systems; formulated a coordinated active-support control scheme comprising adaptive GFM gain and BESS fast frequency response; and quantitatively assessed it on a weakened IEEE 39-bus system with 30a90% renewable penetration. The framework explicitly models the GFM matching-control loop (I_gfm, I_gfm) and the GFL SRF-PLL (I_pll, I_pll) as coupled state variables in the time-domain simulation, so the different dynamic roles of GFM and GFL converters are represented instead of an equivalent inertia constant. The coordinated control scheme was shown to improve maximum RoCoF by up to 22.3% (from 1.038 Hz/s to 0.808 Hz/s at 90%penetration) and increase the frequency nadir by up to 0.27 Hz (from 49.558 Hz to 49.823 Hz), leaving the nadir above the 49.5 Hz UFLS trigger at all levels of penetration. Small-signal modal analysis revealed an apparent upper PLL-bandwidth limit of about 350 rad/s at 90%penetration as compared to 600 at 30%. The Python framework was validated against a benchmark PSS/E simulation of the unaltered IEEE 39-bus system; the absolute metric errors were found to be below 0.05 Hz/s on RoCoF and below Operators with concrete penetration thresholds beyond which additional stability support a in the form of GFM deployment, BESS fast response, or synchronous condensers a becomes mandatory. Three operational recommendations follow from this study. First, GFM control should be made mandatory for at least 50% of converterbased generation at penetration levels above 70%; the 50/50 case in Fig. 6 captured roughly half of the full-GFM benefit at no additional hardware cost. Second, BESS co-located with renewable plants should be operated with a fast frequency-response gain of at least Ka = 10 on system base, and dispatch algorithms should explicitly allocate A+/-10% of headroom for stability support. Third, grid codes should impose penetration-dependent PLL bandwidth restrictions, as depicted by the curves of Fig. 8, to avoid sub-synchronous oscillations at high penetration. There are several directions in which to extend the current work. The three phase steady-state solution will be expanded to unbalanced and weak net conditions through use of a sequence-component converter model. Data-driven estimation methods, including physics-informed neural nets, will be evaluated for the instant estimation of stability margins via PMU data. The BESS model will be incorporated with cell-aging and SOC-dependent power limits; the resultant model will be used to evaluate the longterm economic value of primary frequency response. The framework will then be benchmarked with measurements from a field system, such as Irish or South Australian network with high renewable penetration, to verify the portion models employed here are valid operationalms. "renewables-2024," IEA,Paris, France, 2014. Available: https://www.iea.org/reports/renewables- 2024 grid-forming converters do we need? A perspective," IEEE Trans. EMT system studies for inverter-based resources," North American Electric Reliability Corporation, Atlanta, GA, USA, Tech. Https://www.nerc.com/our-work/guidelines/reliability-guidelines A study on the application of A study on the application of systems utilizing grid-forming converters," Electronics, vol. 14, no. 21, A review of power system stability with high penetration of renewable generation," Int. J. in power systems with high renewable penetration," Renew. Grid-forming energy storage for virtual inertia response, Int. current limiting dynamics for high-IBR power systems, IEEE Trans. Foundations and challenges of low-inertia systems (Invited paper), Proc. 20 th Power Syst. (PSCC), Dublin, Ireland, June 2018, Available at: https://people.ee.ethz.ch/ ~floriand/docs/Articles/PSCC_2018_Survey.pdf Injection "sources and the potential contribution of grid forming converters", European Network of Transmission System Operators for Electricity, Brussels, Belgium, T. Available: file?iid=ECMTMWSyKOPgEwnjWuLMw.. system stability a revisited & extended," IEEE Trans. power converters in AC microgrids," IEEE Trans. Power Electron., vol. The characteristics and representations of synchronous generators," IEEE Trans. Electron., vol. 58, no. 4, pp. Classification of implementations and comparison to droop controllers for microgrids," in Proc. IEEE Grenoble PowerTech, Grenoble, in inverters: An essential element of the power grid," IEEE J. Power system Analysis. Softw., vol. 6, no. 1, art 4, the usefulness of implementing convenient modeling, analysis and optimization of electric power 3(Interconnection of Inverter-Based Resources Interconnecting with Associated Transmission Electric Power Systems), IEEE, New York, NY, https://standards.ieee.org/ieee/2800/14280/

References

[1] International Energy Agency (IEA), *Renewables 2024: Analysis and Forecast to 2030*. Paris, France: IEA, 2024. Available: https://www.iea.org/reports/renewables-2024

[2] F. Milano, F. Dörfler, G. Hug, D. J. Hill, and G. Verbič, "Foundations and challenges of low-inertia systems (Invited paper)," in *Proc. 20th Power Syst. Comput. Conf. (PSCC)*, Dublin, Ireland, Jun. 2018, pp. 1–25. Available: https://people.ee.ethz.ch/~floriand/docs/Articles/PSCC_2018_Survey.pdf

[3] J. Rocabert, A. Luna, F. Blaabjerg, and P. Rodríguez, "Control of power converters in AC microgrids," *IEEE Trans. Power Electron.*, vol. 27, no. 11, pp. 4734–4749, Nov. 2012, doi: 10.1109/TPEL.2012.2199334.

[4] R. H. Lasseter, Z. Chen, and D. Pattabiraman, "Grid-forming inverters: A critical asset for the power grid," *IEEE J. Emerg. Sel. Topics Power Electron.*, vol. 8, no. 2, pp. 925–935, Jun. 2020, doi: 10.1109/JESTPE.2019.2959278.

[5] Q.-C. Zhong and G. Weiss, "Synchronverters: Inverters that mimic synchronous generators," *IEEE Trans. Ind. Electron.*, vol. 58, no. 4, pp. 1259–1267, Apr. 2011, doi: 10.1109/TIE.2010.2048839.

[6] T. Brown, J. Hörsch, and D. Schlachtberger, "PyPSA: Python for power system analysis," *J. Open Res. Softw.*, vol. 6, no. 1, Art. no. 4, 2018, doi: 10.5334/jors.188. Available: https://pypsa.org

[7] North American Electric Reliability Corporation (NERC), *Reliability Guideline: Recommended Practices for Performing EMT System Studies for Inverter-Based Resources*. Atlanta, GA, USA: NERC, Dec. 2024. Available: https://www.nerc.com/our-work/guidelines/reliability-guidelines

[8] L. Thurner et al., "Pandapower—An open-source Python tool for convenient modeling, analysis, and optimization of electric power systems," *IEEE Trans. Power Syst.*, vol. 33, no. 6, pp. 6510–6521, Nov. 2018, doi: 10.1109/TPWRS.2018.2829021.

[9] H. Yang et al., "Stability assessment of fully inverter-based power systems using grid-forming converters," *Electronics*, vol. 14, no. 21, Art. no. 4202, Nov. 2025, doi: 10.3390/electronics14214202.

[10] F. Rodriguez et al., "Review of fast frequency response integration in power systems with high renewable penetration," *Renew. Sustain. Energy Rev.*, vol. 218, Art. no. 114138, 2025, doi: 10.1016/j.rser.2025.114138.

[11] Z. Liu, J. Su, and J. Wang, "Grid-forming converter with enhanced current limiting dynamics for high-IBR power systems," *IEEE Trans. Power Electron.*, vol. 40, no. 3, pp. 3456–3470, Mar. 2025.

[12] P. Kundur, *Power System Stability and Control*, 1st ed. New York, NY, USA: McGraw-Hill, 1994.

[13] S. D'Arco and J. A. Suul, "Virtual synchronous machines—Classification of implementations and analysis of equivalence to droop controllers for microgrids," in *Proc. IEEE Grenoble PowerTech*, Grenoble, France, Jun. 2013, pp. 1–7.

[14] A. R. et al., "Evaluation of the impact of grid forming inverter penetration on power system stability," *Int. J. Emerg. Electr. Power Syst.*, vol. 26, Art. no. 318, 2025, doi: 10.1007/s40866-025-00318-5.

[15] M. Y. Chen, "Composite power-frequency synchronization loop for enhanced grid-forming converter stability," *IEEE Trans. Power Electron.*, vol. 40, no. 1, pp. 1102–1120, Jan. 2025, doi: 10.1109/TPEL.2024.3476452.